

Multidimensional multiplexing holography based on optical orbital angular momentum lattice multiplexing

Tian Xia,^a Zhenwei Xie^{✉,a,*} and Xiaocong Yuan^{a,b,*}

^aShenzhen University, Institute of Microscale Optoelectronics, Nanophotonics Research Centre, State Key Laboratory of Radio Frequency Heterogeneous Integration, Shenzhen, China

^bResearch Institute of Intelligent Sensing, Research Center for Humanoid Sensing, Zhejiang Lab, Hangzhou, China

Abstract. The use of orbital angular momentum (OAM) as an independent dimension for information encryption has garnered considerable attention. However, the multiplexing capacity of OAM is limited, and there is a need for additional dimensions to enhance storage capabilities. We propose and implement orbital angular momentum lattice (OAML) multiplexed holography. The vortex lattice (VL) beam comprises three adjustable parameters: the rotation angle of the VL, the angle between the wave normal and the z axis, which determines the VL's dimensions, and the topological charge. Both the rotation angle and the VL's dimensions serve as supplementary encrypted dimensions, contributing azimuthally and radially, respectively. We investigate the mode selectivity of OAML and focus on the aforementioned parameters. Through experimental validation, we demonstrate the practical feasibility of OAML multiplexed holography across multiple dimensions. This groundbreaking development reveals new possibilities for the advancement of practical information encryption systems.

Keywords: orbital angular momentum lattice multiplexed holography; vortex lattice beam; information encryption.

Received Oct. 10, 2023; revised manuscript received Nov. 22, 2023; accepted for publication Dec. 5, 2023; published online Jan. 3, 2024.

© The Authors. Published by SPIE and CLP under a Creative Commons Attribution 4.0 International License. Distribution or reproduction of this work in whole or in part requires full attribution of the original publication, including its DOI.

[DOI: [10.1117/1.APN.3.1.016005](https://doi.org/10.1117/1.APN.3.1.016005)]

1 Introduction

Optical holography technology utilizes computer-generated holograms to reconstruct the beam field, achieving remarkable success across various applications, such as data storage, 3D printing, artificial intelligence, and optical tweezers.¹⁻⁴ However, traditional holography is limited by polarization, wavelength, and incident angle as independent multiplexing channel parameters.⁵⁻¹¹ This approach is constrained by limited spatial channel availability and significant cross talk. To overcome these limitations, the use of optical orbital angular momentum (OAM) as an additional information bearer in holography has gained increasing attention.¹²⁻¹⁵

OAM collection is distinguished by its angular vortex phases, providing an endless array of unique mode channels

for multiplexing.¹⁶⁻¹⁸ Recent developments have showcased practical implementations of OAM multiplexed holography, establishing it as a standalone information channel.¹²⁻¹⁴ This technique retains the OAM property and enables selective image reconstruction based on the encoded OAM. Various forms of OAM holography have emerged, such as polarization-encrypted OAM holography, ellipticity-encrypted OAM holography, ultradense perfect OAM multiplexed holography, partial OAM holography, modulated OAM holography, multiple-image and multiple-dimensional encrypted OAM multiplexed holography, and holographic strategy for OAM that incorporates complex features by employing deep-learning algorithms.¹⁹⁻²⁷

Despite these advancements, the capacity for encoded information in OAM multiplexed holography remains limited. Moreover, conventional OAM multiplexed holography lacks an additional degree of freedom to enhance both information security and capacity. A newly proposed approach, MHC-OAM multiplexed holography, introduces new degrees of freedom by

*Address all correspondence to Zhenwei Xie, ayst31415926@szu.edu.cn; Xiaocong Yuan, xcyuan@szu.edu.cn

multiplexing different angular momentum modes of light beams, enabling the simultaneous transmission of multiple information channels.²⁸ Overall, the use of OAM in holography has the potential to revolutionize information transmission and storage, and ongoing research seeks to further optimize this technology.

In this study, we introduce and demonstrate the effectiveness of orbital angular momentum lattice (OAML) multiplexed holography, an innovative technique that utilizes a vortex lattice (VL) beam that is independently adjustable within three crucial parameters: the rotation angle of the VL, the angle between the wave normal and the z axis (which determines the VL's size), and the topological charge. Notably, the rotation angle and the size of the VL introduce additional encrypted dimensions, specifically in the azimuthal and radial directions. We conduct an extensive investigation into the selectivity of OAML modes based on these parameters, enabling us to achieve multidimensional multiplexed holography. Our experimental results affirm the practicality of OAML multiplexed holography across various dimensions, holding significant promise in the field of information encryption. This methodology unlocks new possibilities for robust optical encryption and a wide range of classical or quantum information applications.

2 Materials and Methods

The proposed VL beam significantly enhances the encryption capacity of OAM holography. Figure 1 shows a comparison between OAML holography and conventional OAM holography. In the case of the conventional OAM beam [top of Fig. 1(a)], an OAM-preserved hologram is designed to maintain the OAM

property of incident OAM beams in each pixel of reconstructed holographic images, allowing OAM to serve as an independent information carrier. Conversely, for the VL beam, the rotation angle of the VL, the angle between the wave normal and the z axis, and the topological charges are configured as independent information carriers. In the upper part of Fig. 1(b), a helical phase plate is overlaid with an OAM-preserved hologram to create an OAM-selective hologram for the conventional OAM beam. This hologram contains spatial-frequency components that carry a helical wavefront. Due to OAM conservation, only a specific incident OAM beam with an inverse helical mode index can be transformed into a Gaussian mode, selectively reconstructing a holographic image encoded in an OAM image channel. Similarly, for the VL beam, when a VL phase is added to an OAM-preserved hologram, an OAM-selective hologram is achieved. It is worth noting that for the OAML-preserved hologram, different hologram images correspond to different VLs with varying rotation angles and sizes in the Fourier plane. The different VLs with different rotation angles correspond to different points on the same circle, while the different VLs with different sizes correspond to various points on concentric rings with different radii. As these different points on the concentric ring or the single circle are orthogonal, the aforementioned VLs are also orthogonal (see Supplementary Note 1 in the [Supplementary Material](#)). This hologram likewise contains spatial-frequency components. Due to the conservation of OAM, only a specific incident VL beam, with its topological charge reversed compared to the topological charge at the back focal plane of the lens for the OAM-selective hologram, can be transformed into a Gaussian mode in the Fourier transform plane.

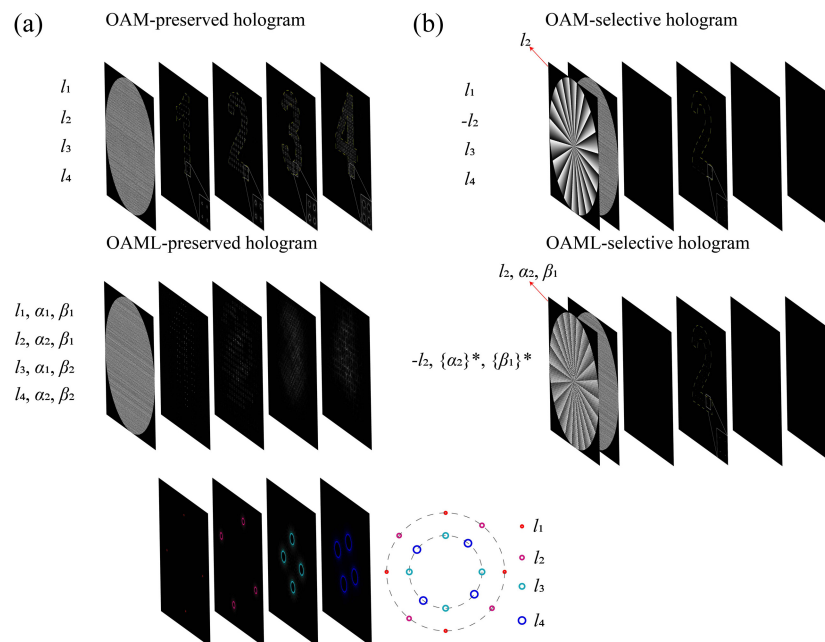


Fig. 1 Schematic diagrams of two types of holograms: (a) an OAM-preserved hologram and (b) an OAM-selective hologram. These holograms are designed to transfer the OAM property from an incident OAM beam to a holographic image and to reconstruct specific OAM channels, respectively. Top: the conventional OAM beam. Bottom: the proposed VL beam. $\{a_1\}^*$ and $\{\beta_1\}^*$ are the equivalent values of α_2 and β_1 for the conjugate phase of the encoded phase, respectively.

The VL phase φ generating the VL beam can be calculated as

$$\varphi = \arg \left\{ \left[\exp \left(ik \frac{x+y \tan \alpha}{\sqrt{1+\tan^2 \alpha}} \sin \beta \right) + \exp \left(ik \frac{-x+y \tan(-\alpha)}{\sqrt{1+\tan^2(-\alpha)}} \sin \beta \right) + \exp \left(ik \frac{y+x \tan(-\alpha)}{\sqrt{1+\tan^2(-\alpha)}} \sin \beta \right) + \exp \left(ik \frac{-y+x \tan \alpha}{\sqrt{1+\tan^2 \alpha}} \sin \beta \right) \right] \cdot \exp(il\theta) \right\}, \quad (1)$$

where $k = 2\pi/\lambda$, λ is the wavelength set as 532 nm in this paper, (x, y) represents the rectangular coordinate, and α , β , l , and θ present the rotation angle of the VL, the angle between the wave normal and the z axis, topological charge, and azimuth angle, respectively. As the chosen example is the VL, which is the quadruple rotational symmetry, α ranges from 0 to $\pi/2$. β is too large to make the four holographic images overlap, which identifies the encrypted image and cannot achieve the image encryption. β should have a small value and determines the size of the VL. To simplify matters, this paper chooses the square VL as an example, even though the VL can have an arbitrary shape.

The spatial-frequency distribution of the VL beams based on the Fourier integral theorem is expressed as

$$u = \int_0^{2\pi} \int_0^\infty \text{circ}(r/R) \exp(i\varphi) \exp[-i2\pi r \rho \cos(\theta - \phi)] r dr d\theta, \quad (2)$$

where $\text{circ}(r/R)$ is the circle function used to describe the circular aperture stop, r and R represent the radial coordinate and the normalization factor of the radial coordinate, respectively, and (ρ, ϕ) indicate the polar coordinates in the image plane.

In computer-generated holography, a Fourier pair is established between the electric field in the image plane and the holographic plane. As a result, the electric field of the reconstructed image is

$$E^{\text{OAM}} = \mathfrak{F}[E_h \cdot E^{\text{OAM}}] = \mathfrak{F}[E_h] * \mathfrak{F}[E^{\text{OAM}}], \quad (3)$$

where E_h and E^{OAM} are the complex amplitudes of the hologram and the VL beam, respectively. The operators \mathfrak{F} and $*$ are the Fourier transform and convolution, respectively. If the sampling array of the target image is correlated with the spatial frequency of the VL-OAM beam, the OAM properties will be preserved in the reconstructed image.

The design principle of OAML holography is visually depicted in Fig. 2(a). Employing the Gerchberg–Saxton (GS) algorithm, we obtain an OAM-preserved hologram, as demonstrated in the middle section of Fig. 2(a). To achieve clear reconstructed images, we set “ d ” in the 2D Dirac comb to 184 μm for this study. It is important to note that the VL beam is preserved in each pixel of the reconstructed image. In the right

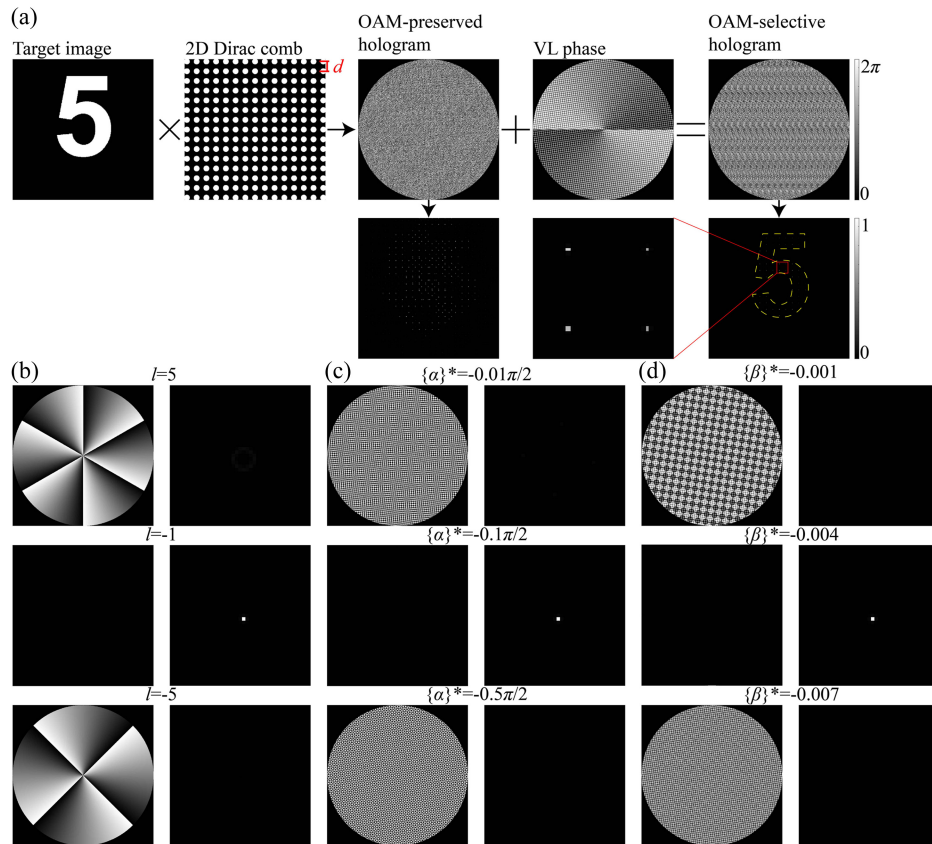


Fig. 2 OAML mode selectivity. (a) Design concept for an OAM-preserved hologram and an OAM-selective hologram. (b) Mode selectivity of the constant l . (c) Mode selectivity of α . (d) Mode selectivity of β .

portion of Fig. 2(a), we superimpose the phase function φ of a VL beam with ($l = 1, \alpha = 0.1\pi/2, \beta = 0.004$) onto the OAM-preserved hologram, resulting in the creation of an OAM-selective hologram. Due to the conservation of OAM, only a specific incident VL beam with ($l = -1, \{\alpha\}^* = -0.1\pi/2, \{\beta\}^* = -0.004$) can produce Gaussian spots with a stronger intensity distribution in the desired holographic image. Consequently, we obtain the multiplexed hologram. The mode selectivity of VL beams in image reconstruction is shown in Figs. 2(b)–2(d) and takes into account different values of “ l ,” “ α ,” and “ β .” The encoded phase parameters of the hologram remain fixed at ($l = 1, \alpha = 0.1\pi/2, \beta = 0.004$). First, we demonstrate the mode selectivity of VL beams while keeping “ α ” and “ β ” constant, as presented in Fig. 2(b). When the hologram is illuminated by the decoded phase mode ($l = -1, \{\alpha\}^* = -0.1\pi/2, \{\beta\}^* = -0.004$), a Gaussian spot with stronger intensity is obtained. However, when the incident-decoded VL beam has values of ($l = 5, -5, \{\alpha\}^* = -0.1\pi/2, \{\beta\}^* = -0.004$), compared to Gaussian spots under the above correct incident-decoded VL beam, the reconstructed light field exhibits lower intensity. Figure 2(c) illustrates the impact of “ α ” on the mode selectivity. Similarly, when the hologram is illuminated by the decoded phase mode ($l = -1, \{\alpha\}^* = -0.1\pi/2, \{\beta\}^* = -0.004$), the desired Gaussian spot is obtained. On the other hand, the peak intensity of the mode with values of ($l = -1, \{\alpha\}^* = -0.01\pi/2, 0.5\pi/2, \{\beta\}^* = -0.004$) is lower than that of the mode with ($l = -1, \alpha^* = -0.1\pi/2, \{\beta\}^* = -0.004$). Figure 2(d) shows the effect of “ β ” on the mode selectivity. Once again, when the hologram is illuminated by the decoded phase mode ($l = -1, \{\alpha\}^* = -0.1\pi/2, \{\beta\}^* = -0.004$), the desired Gaussian spot is obtained. Conversely, the peak intensity of the mode with values of ($l = -1, \{\alpha\}^* = -0.1\pi/2, \{\beta\}^* = -0.001, 0.007$) is lower than that of the mode with ($l = -1, \{\alpha\}^* = -0.1\pi/2, \{\beta\}^* = -0.004$). In Figs. 2(b)–2(d), the phase depicted is the combined result of the fixed encoded phase and the phase of the incident-decoded VL beam. Therefore, when the phase of the incident-decoded VL beam aligns perfectly with the correct decoded phase of the fixed encoded phase, the phase in Fig. 2 becomes zero. In other words, the entire superimposed phase appears as totally black.

3 Results and Discussion

The experimental setup for OAML holography is presented in Fig. 3. We employ a laser with a wavelength of 532 nm as the light source. To ensure optimal beam characteristics, we expand and collimate the laser beam using a spatial filter comprising an objective lens, a pinhole, and an additional lens to adjust the incident beam size, aligning it with the phase-only spatial light modulator (SLM, UPOLabs-HDSL80R Pro, 1920 pixels \times 1200 pixels, pixel pitch of 8 μm). Since the SLM is sensitive solely to the horizontally polarized component of the incident beam, we insert a polarizer between the spatial filter and the SLM, generating a horizontally polarized beam. The modulated beam, reflected by the beam splitter, is directed through a CMOS camera (FLIR, GS3-U3-123S6C-C, 4096 pixels \times 3000 pixels, pixel pitch of 3.45 μm) responsible for capturing the reconstructed holographic image. In this specific experiment, the system is simplified, as only one SLM is utilized. Rather than directly illuminating the hologram pattern with a VL beam, we superimpose the decoded VL phase distribution onto the hologram. The hologram itself is then illuminated by

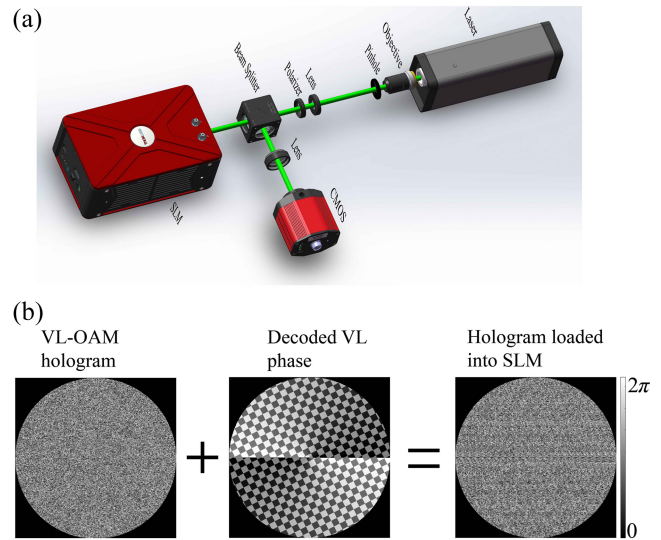


Fig. 3 (a) Schematic diagram of the experimental setup of OAML hologram. (b) The hologram loaded into the SLM consists of two components: the decoded phase and the OAM hologram.

a planar beam, as shown in Fig. 3(a). During the decryption process, the hologram can be represented as the superposition of the decoded VL phase and the OAML hologram. Therefore, the mathematical representation of the phase-only hologram can be described as

$$P = \arg \left[\sum_{i=1}^N \exp(i\Phi_i) \exp(i\psi_{i-de}) \right], \quad (4)$$

where Φ_i represents the phase information of each image channel, ψ_{i-de} represents the decoded VL phase distribution, and N represents the number of multiplexing channels. The design principle of the hologram loaded into the SLM is shown in Fig. 3(b). We’ve thoroughly analyzed the impact of adding another SLM, factoring in misalignment (see Supplementary Note 2 in the [Supplementary Material](#)).

Figure 4 provides a visual representation of the schematic diagram that elucidates the concept of l -encrypted OAML multiplexed holography. The experimental setup involves encoding four distinct target images labeled as Arabic numerals “1,” “2,” “3,” and “4” into separate holograms while preserving crucial OAM information. This encoding process utilizes the GS algorithm to achieve optimal results. To accomplish this, we employ four VL phase modes, each characterized by specific parameters, denoted as ($l = 1, 11, 21, 31, \alpha = 0.2\pi/2, \{ \beta \} = 0.2\pi/2, 0.2\pi/2, 0.2\pi/2, \beta = 0.001, 0.001, 0.001, 0.001$). These parameters enable the creation of corresponding OAM-selective holograms. These individual holograms are then combined to produce a unified OAM multiplexed hologram, as shown in Fig. 4(a). To assess the practical feasibility of l -multiplexed holography, we conducted both numerical simulations and physical experiments, as meticulously presented in Figs. 4(b)–4(e). During the experimental phase, the OAML multiplexed hologram associated with a specific “ l ” key was subjected to various incident VL beams. These beams were characterized by parameters such as ($l = -1, \{\alpha\}^* = -0.2\pi/2, \{\beta\}^* = -0.001$), ($l = -11, \{\alpha\}^* = -0.2\pi/2, \{\beta\}^* = -0.001$), ($l = -21, \{\alpha\}^* = -0.2\pi/2, \{\beta\}^* = -0.001$), and ($l = -31,$

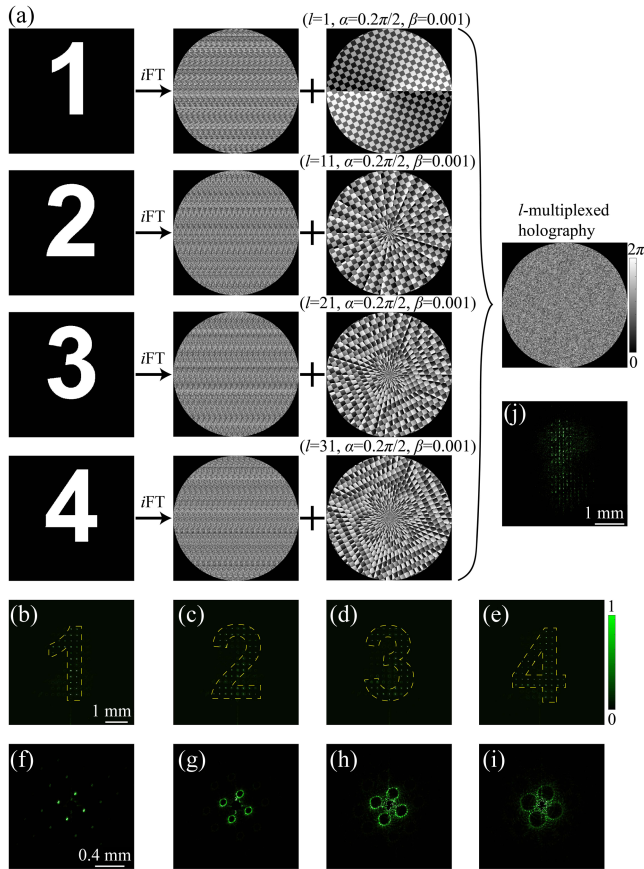


Fig. 4 Schematic diagram of OAML multiplexed holography designed with key l . (a) Design process. (b)–(e) Experimental reconstruction results based on the l -dependence of the incident VL beams with $(l = -1, -11, -21, -31, \{\alpha\}^* = -0.2\pi/2, -0.2\pi/2, -0.2\pi/2, -0.2\pi/2, \{\beta\}^* = -0.001, -0.001, -0.001, -0.001)$, respectively. (f)–(i) Capture intensity distributions of the above VL beams, respectively. (j) Experimental reconstruction results of the OAML-preserved holography.

$\{\alpha\}^* = -0.2\pi/2, \{\beta\}^* = -0.001)$. Intriguingly, this arrangement resulted in the reconstruction of four distinct images: “1,” “2,” “3,” and “4” at the lens’s focal plane for each corresponding case. Consequently, these results conclusively demonstrate the effectiveness of utilizing specific “ l ” values associated with incident VL beams to achieve the encryption of four discrete images from a single multiplexed hologram. Figures 4(f)–4(i) illustrate the capture intensity distributions of the aforementioned VL beams, respectively. Upon illumination of the multiplexed OAML-preserved hologram by a planar beam, four images manifest simultaneously, appearing indistinguishable from each other, as shown in Fig. 4(j). Let us consider the case of OAML holography, which encodes singular OAM information to produce a single image. In this scenario, we employ a blazed grating to modulate the phase of the holography, allowing us to selectively extract the first-order diffraction through the SLM. Within the experimental framework, the efficiency of both generating and decoding the holography is quantified by the ratio between the energy content of the reconstructed image and that of the background. While the measured efficiency currently stands at 12.95%, it is possible to optimize the experimental setup further to bring it closer to its numerical simulation value of 71.84%.

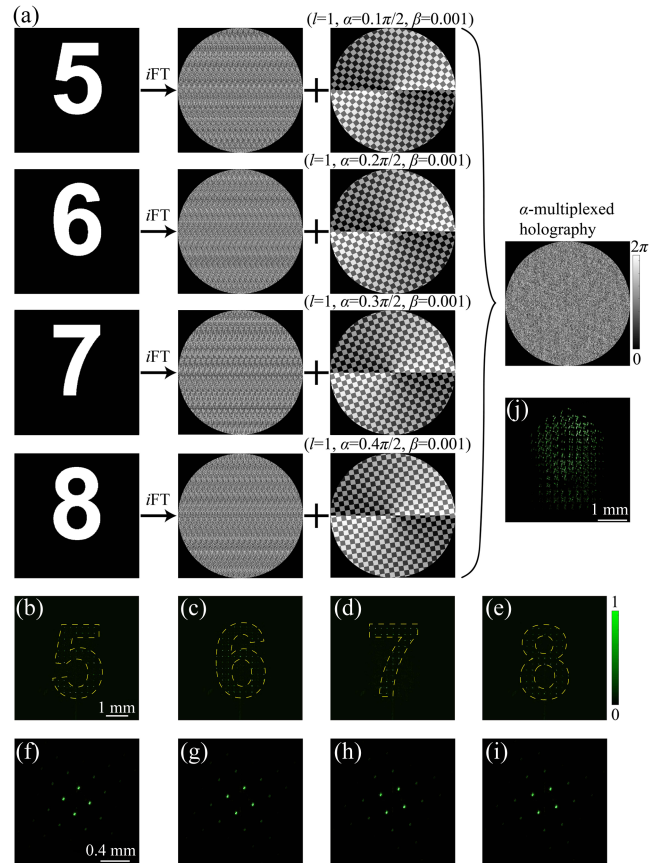


Fig. 5 Schematic diagram of OAML multiplexed holography designed with key α . (a) Design process. (b)–(e) Experimental reconstruction results based on the α -dependence of the incident VL beams with $(l = -1, -1, -1, -1, \{\alpha\}^* = -0.1\pi/2, -0.2\pi/2, -0.3\pi/2, -0.4\pi/2, \{\beta\}^* = -0.001, -0.001, -0.001, -0.001)$, respectively. (f)–(i) Capture intensity distributions of the above VL beams, respectively. (j) Experimental reconstruction results of the OAML-preserved holography.

Figure 5 provides a schematic diagram of α -encrypted OAML multiplexed holography. In this setup, four target images, represented by Arabic numerals “5,” “6,” “7,” and “8” are individually encoded into four holograms while preserving the OAM information. Specifically, four VL phase modes with parameters $(l = 1, 1, 1, 1, \alpha = 0.1\pi/2, 0.2\pi/2, 0.3\pi/2, 0.4\pi/2, \beta = 0.001, 0.001, 0.001, 0.001)$ are used to generate the corresponding OAM-selective holograms. These four OAM-selective holograms can be superimposed to form a single OAM multiplexed hologram, as shown in Fig. 5(a). To evaluate the feasibility of α -multiplexed holography, we conducted numerical simulations and presented the experimental results in Figs. 5(b)–5(e). In these experiments, the OAML multiplexed hologram with the specific α key is illuminated by different incident VL beams. When the OAML multiplexed hologram with the α key is illuminated by different incident VL beams with $(l = -1, \{\alpha\}^* = -0.1\pi/2, \{\beta\}^* = -0.001)$, $(l = -1, \{\alpha\}^* = -0.2\pi/2, \{\beta\}^* = -0.001)$, $(l = -1, \{\alpha\}^* = -0.3\pi/2, \{\beta\}^* = -0.001)$, and $(l = -1, \{\alpha\}^* = -0.4\pi/2, \{\beta\}^* = -0.001)$, four distinct images “5,” “6,” “7,” and “8” are reconstructed at the focal plane of the lens, respectively. These results demonstrate that by utilizing specific α values associated with the incident VL beams, four

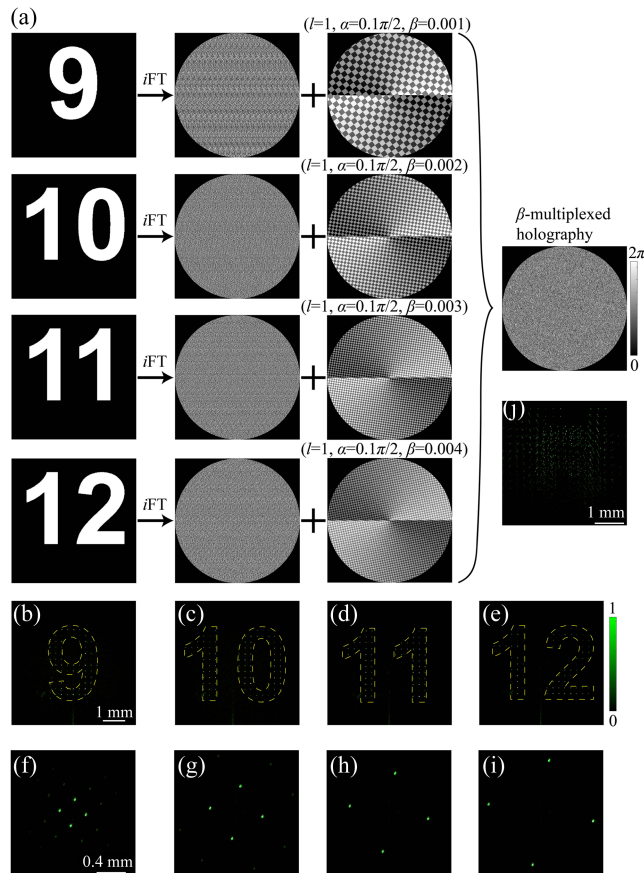


Fig. 6 Schematic diagram of OAML multiplexed holography designed with key β . (a) Design process. (b)–(e) Experimental reconstruction results based on the β -dependence of the incident VL beams with $(l = -1, -1, -1, -1, \{\alpha\}^* = -0.1\pi/2, -0.1\pi/2, -0.1\pi/2, -0.1\pi/2, \{\beta\}^* = -0.001, -0.002, -0.003, -0.004)$, respectively. (f)–(i) Capture intensity distributions of the above VL beams, respectively. (j) Experimental reconstruction results of the OAML-preserved holography.

images can be effectively encrypted from a single multiplexed hologram. Figures 5(f)–5(i) illustrate the capture intensity distributions of the aforementioned VL beams, respectively. Upon illumination of the multiplexed OAML-preserved hologram by a planar beam, four images manifest simultaneously, appearing indistinguishable from each other, as depicted in Fig. 5(j).

Figure 6 presents a schematic diagram of β -encrypted OAML multiplexed holography. In this configuration, four target images represented by Arabic numerals “9,” “10,” “11,” and “12” are individually encoded into four holograms while preserving the OAM information. Specifically, four VL phase modes with parameters $(l = 1, 1, 1, 1, \alpha = 0.1\pi/2, 0.1\pi/2, 0.1\pi/2, 0.1\pi/2, \beta = 0.001, 0.002, 0.003, \text{ and } 0.004)$ are utilized to generate the corresponding OAM-selective holograms. These four OAM-selective holograms can be superimposed to form a single OAM multiplexed hologram, as depicted in Fig. 6(a). To evaluate the feasibility of β -multiplexed holography, we conducted numerical simulations and presented the experimental results in Figs. 6(b)–6(e). In these experiments, the OAML multiplexed hologram with the specific β key is illuminated by different incident VL beams. When the OAML multiplexed hologram with

the β key is illuminated by the different incident VL beams with $(l = -1, \{\alpha\}^* = -0.1\pi/2, \{\beta\}^* = -0.001)$, $(l = -1, \{\alpha\}^* = -0.1\pi/2, \{\beta\}^* = -0.002)$, $(l = -1, \{\alpha\}^* = -0.1\pi/2, \{\beta\}^* = -0.003)$, and $(l = -1, \{\alpha\}^* = -0.1\pi/2, \{\beta\}^* = -0.004)$, four distinct images “9,” “10,” “11,” and “12” are reconstructed at the focal plane of the lens, respectively. These results demonstrate that by utilizing the specific β values associated with the incident VL beams, four images can be effectively encrypted from a single multiplexed hologram. Figures 6(f)–6(i) illustrate the capture intensity distributions of the aforementioned VL beams, respectively. Upon illumination of the multiplexed OAML-preserved hologram by a planar beam, four images manifest simultaneously, appearing indistinguishable from each other, as shown in Fig. 6(j). We also have studied the multiple parameters OAML multiplexed hologram (see Supplementary Notes 3–6 in the [Supplementary Material](#)).

4 Conclusion

In this study, we introduced OAML multiplexed holography as an innovative approach to enhance holographic multiplexing capabilities. Our method involves modulating key parameters, including the rotation angle of the square lattice, the angle between the wave normal and the z axis (which determines the size of the square lattice), and the topological charge. By manipulating these parameters, we achieved multidimensional multiplexing within holography. It is worth noting that these parameters are mutually orthogonal, allowing for independent control. Furthermore, we conducted a comprehensive investigation into the selectivity of the OAML mode based on the aforementioned parameters, enabling efficient multiplexing in holography. Experimental verification unequivocally demonstrated the feasibility of OAML multiplexed holography and its potential applications in enhancing information encryption. This significant advancement in multiplexed holography holds great promise for various fields, including optical communication, optical encryption, and 3D display.

Code and Data Availability

Data underlying the results presented in this paper can be obtained from the authors upon reasonable request.

Acknowledgments

This research was supported by the Guangdong Major Project of Basic and Applied Basic Research (Grant No. 2020B0301030009), the National Natural Science Foundation of China (Grant Nos. 61935013, 62375181, and 61975133), the Shenzhen Science and Technology Program (Grant No. JCYJ20200109114018750), and the Shenzhen Peacock Plan (Grant No. KQTD20170330110444030).

References

1. J. F. Heanue, M. C. Bashaw, and L. Hesselink, “Volume holographic storage and retrieval of digital data,” *Science* **265**(5173), 749–752 (1994).
2. K. T. P. Lim et al., “Holographic colour prints for enhanced optical security by combined phase and amplitude control,” *Nat. Commun.* **10**(1), 25 (2019).
3. X. Lin et al., “All-optical machine learning using diffractive deep neural networks,” *Science* **361**(6406), 1004–1008 (2018).
4. K. Dholakia and T. Čížmár, “Shaping the future of manipulation,” *Nat. Photonics* **5**(6), 335–342 (2011).

5. S. M. Kamali et al., "Angle-multiplexed metasurfaces: encoding independent wavefronts in a single metasurface under different illumination angles," *Phys. Rev. X* **7**(4), 041056 (2017).
6. J. P. Balthasar Mueller et al., "Metasurface polarization optics: independent phase control of arbitrary orthogonal states of polarization," *Phys. Rev. Lett.* **118**(11), 113901 (2017).
7. X. Li et al., "Athermally photoreduced graphene oxides for three-dimensional holographic images," *Nat. Commun.* **6**(1), 6984 (2015).
8. Q. Xu et al., "Meta-optics inspired surface plasmon devices," *Photonics Insights* **2**(1), R02 (2023).
9. Q. Ma et al., "Information metasurfaces and intelligent metasurfaces," *Photonics Insights* **1**(1), R01 (2022).
10. D. Wen et al., "Light field on a chip: metasurface-based multicolor holograms," *Adv. Photonics* **3**(2), 024001 (2021).
11. J. Kim et al., "Tunable metasurfaces towards versatile metalenses and metaholograms: a review," *Adv. Photonics* **4**(2), 024001 (2022).
12. H. Ren et al., "Metasurface orbital angular momentum holography," *Nat. Commun.* **10**(1), 2986 (2019).
13. X. Fang, H. Ren, and M. Gu, "Orbital angular momentum holography for high-security encryption," *Nat. Photonics* **14**(2), 102–108 (2020).
14. H. Ren et al., "Complex-amplitude metasurface-based orbital angular momentum holography in momentum space," *Nat. Nanotechnol.* **15**(11), 948–955 (2020).
15. Q. Cao et al., "Propagation of transverse photonic orbital angular momentum through few-mode fiber," *Adv. Photonics* **5**(3), 036002 (2023).
16. R. Zhao, L. Huang, and Y. Wang, "Recent advances in multi-dimensional metasurfaces holographic technologies," *Photonix* **1**, 20 (2020).
17. X. Fang et al., "High-dimensional orbital angular momentum multiplexing nonlinear holography," *Adv. Photonics* **3**(1), 015001 (2021).
18. H. Yang et al., "Angular momentum holography via a minimalist metasurface for optical nested encryption," *Light Sci. Appl.* **12**(1), 79 (2023).
19. H. Zhou et al., "Polarization-encrypted orbital angular momentum multiplexed metasurface holography," *ACS Nano* **14**(5), 5553–5559 (2020).
20. P. Cheng, S. Huang, and C. Yan, "Ellipticity-encrypted orbital angular momentum multiplexed holography," *J. Opt. Soc. Am. A* **38**(12), 1875–1883 (2021).
21. G. Zhu et al., "Ultra-dense perfect optical orbital angular momentum multiplexed holography," *Opt. Express* **29**(18), 28452–28460 (2021).
22. F. Wang et al., "Angular multiplexation of partial helical phase modes in orbital angular momentum holography," *Opt. Express* **30**(7), 11110–11119 (2022).
23. F. Wang et al., "Enhancing the information capacity with modulated orbital angular momentum holography," *IEEE Photonics J.* **14**(1), 5212905 (2022).
24. F. Li et al., "Multiple-dimensional multiplexed holography based on modulated chiro-optical fields," *Opt. Express* **30**(23), 41567–41579 (2022).
25. F. Li et al., "Multiple-image encryption using phase jump gradient factors -based OAM multiplexing holography," *Opt. Lasers Eng.* **160**, 107303 (2023).
26. Z. Huang et al., "Orbital angular momentum deep multiplexing holography via an optical diffractive neural network," *Opt. Express* **30**(4), 5569–5584 (2022).
27. F. Feng et al., "Deep learning-enabled orbital angular momentum-based information encryption transmission," *ACS Photonics* **9**(3), 820–829 (2022).
28. N. Zhang et al., "Multiparameter encrypted orbital angular momentum multiplexed holography based on multiramp heliconical beams," *Adv. Photonics Nexus* **2**(3), 036013 (2023).

Tian Xia is a postdoc at the Institute of Microscale Optoelectronics at Shenzhen University. His research interests include zone plate, beam control, holography, and metasurface.

Zhenwei Xie is an associate professor at the Institute of Microscale Optoelectronics at Shenzhen University. He specializes in using metasurfaces and inverse design methods to control the orbital and spin angular momentum of light, and applies these techniques to fields such as mode-division multiplexing optical communication and on-chip photonic devices. He has published over 70 SCI-indexed papers in prestigious journals, such as *Light: Science & Applications*, *Physical Review Letters*, *Laser & Photonics Review*, *ACS Photonics*, and *Photonics Research*. He was listed by Stanford University as one of the "World's Top 2% Scientists" in an annual scientific impact ranking (2022). He has received Top Downloaded Paper awards for five papers, and one paper has been recognized as a Highly Cited Paper by ESI. His work has been cited 3213 times on Google Scholar, with an H-index of 27.

Xiacong Yuan is Changjiang Scholar Professor and director of the Nanophotonics Research Center at Shenzhen University. He received his PhD in physics from King's College London in 1994. He is now a fellow of SPIE and Optica and a board member of the Chinese Optical Society and the Chinese Optical Engineering Society. His research interests include singular optics, nanophotonics, plasmonics, advanced light manipulations, and their applications in communications, imaging, and optical tweezers.